Electronic Supplementary Material (ESI) for Analyst.


# Supporting Information: Enabling the characterization of the nonlinear electrokinetic properties of particles using low voltage

J. Martin de los Santos-Ramirez,[1] Carlos A. Mendiola-Escobedo,[1] Jose M. Cotera-Sarabia,[1] Roberto C. Gallo-Villanueva,[1] Rodrigo Martinez-Duarte,[2]* Víctor H. Perez-Gonzalez[1]*

[1]School of Engineering and Sciences, Tecnologico de Monterrey, Av. Eugenio Garza Sada 2501, Monterrey NL, 64700, Mexico.

[2] Multiscale Manufacturing Laboratory, Department of Mechanical Engineering, Clemson University, Clemson, SC 29634, USA.

*Correspondence should be addressed to:

**Victor H. Perez-Gonzalez, PhD**

School of Engineering and Sciences

Tecnologico de Monterrey, Monterrey NL, 64700, Mexico

vhpg@tec.mx

**Rodrigo Martinez-Duarte, PhD**

Department of Mechanical Engineering

Clemson University, Fluor Daniel Building, Clemson, S.C. 29634

rodrigm@clemson.edu

## 1. COMSOL modelling

### 1.1 COMSOL model parameters, domains, and boundary conditions

The Electric Currents interface from the AC/DC module was used for solving all electric related phenomena, and the Creeping Flow interface from the Fluid Flow module was used for the fluid transport related phenomena in a 2D model. Figure S1A shows a representation of the system used for numerical analysis with all relevant physical domain and boundary conditions used for the model for both electrical and fluid transport physics. Note that in the total particle velocity, $u_p$, the electroosmotic velocity, $u_{EO}$, is replaced by the COMSOL reserved variable, spf.U, as it represents the electroosmotic flow field velocity due momentum transfers from $u_{slip}$ on the channel walls to the fluid bulk. For the geometry meshing, a custom free triangular mesh was used. The maximum element size was set to 50 µm while the minimum element size was set to 0.5 µm, at the same time, a minimum size exclusive zone was set on the region of interest, i.e., triangle gap, as shown by the dashed square in the center of Fig. S1A. A representation of the mesh can be seen in Fig. S1B. Note that Fig. S1B is just a representation of the actual mesh, this is because showing the actual mesh will result in a totally black filled rectangle due to the mesh refinement.

In addition, Table S1 shows all the needed parameters for computing the total particle velocity due to the combination of all treated electrokinetic phenomena.

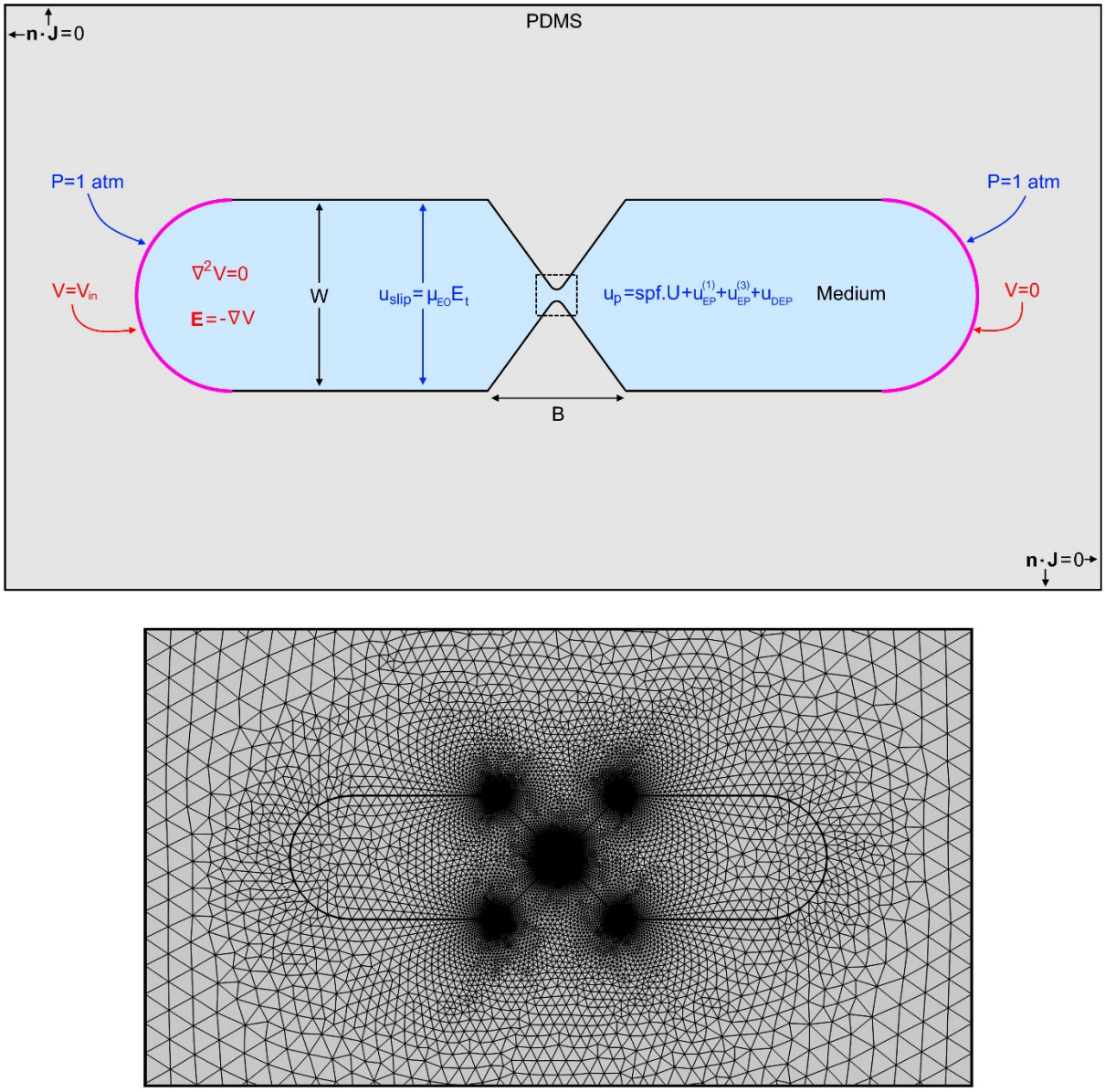


**Figure S1** System representation for numerical modeling. **(A)** Domains and boundary conditions for solving electric and fluid physics. **(B)** Representation of the resulting model meshing process.

**Table S1** COMSOL parameters used for the numerical simulations.

| Parameter | Symbol | Value | Units |
|---|---|---|---|
| Electroosmotic mobility | $\mu_{EO}$ | $7.28\times10^{-8}$ | $m^2/V\cdot s$ |
| Linear electrophoretic mobility | $\mu_{EP}^{(1)}$ | $-8.81\times10^{-9}$ | $m^2/V\cdot s$ |
| Nonlinear electrophoretic mobility | $\mu_{EP}^{(3)}$ | $-3.51\times10^{-18}$ | $m^4/V^3\cdot s$ |
| Dielectrophoretic mobility | $\mu_{DEP}$ | $1.65\times10^{-19}$ | $m^4/V^2\cdot s$ |
| Medium relative permittivity | $\varepsilon_m$ | 80 | - |
| PDMS relative permittivity | $\varepsilon_{PDMS}$ | 2.75 | - |
| Medium conductivity | $\sigma_m$ | $2.5\times10^{-4}$ | S/m |
| Particle conductivity | $\sigma_p$ | $20\times10^{-4}$ | S/m |
| PDMS conductivity | $\sigma_{PDMS}$ | $8.33\times10^{-13}$ | S/m |
| Clausius-Mossotti factor | $Re[K(\omega)]$ | 0.7 | - |
| Medium viscosity | $\eta$ | 0.001 | Pa·s |
| Reference temperature | $T_0$ | 293.15 | K |
| Channel width | W | 1000-4000 | µm |
| Triangle base | B | 0-4000 | µm |
| Triangle base/channel width ratio | $\xi$ | 0-2.5 | - |
| *Medium 3D extrusion | - | 30 | µm |
| *PDMS 3D extrusion | - | 5000 | µm |
| *Glass 3D extrusion | - | 1500 | µm |

*For 3D model only

### 1.2 Comparing 2D vs 3D COMSOL model electric behavior

A 3D version of the model (design 4) was constructed to evaluate the validity of using a 2D model for all design cases. All physics, configuration parameters and boundary conditions were translocated from the 2D model. Figure S2 shows the schematic comparing the 3D model (Figure S2A) and the 2D model (Figure S2B). Figures S2C and D show the electric field magnitude distribution on a middle cut plane in the center of the microchannel for the 3D model and the electric field magnitude for the 2D in the same region, respectively. From Figures S2C and D the difference in the electric field distribution is indistinguishable from one another. However, it is possible to compare the maximum values for each model (2302 V/cm for the 3D and 2298 V/cm for the 2D) resulting in a relative percentage difference of just 0.17 %. With this, it is fair to conclude that the use of 2D models, instead of 3D ones, to analyze the electric field distribution within DC-iEK devices like the ones presented herein is well justified. Moreover, because electrokinetic phenomena depend on the distribution of the electric field, no significant difference might arise when using 2D models. Furthermore, the use of 2D models reduces the model complexity, computing time (~2 h and 30 min for 3D model vs ~7 min for the 2D model), and computational resources usage.

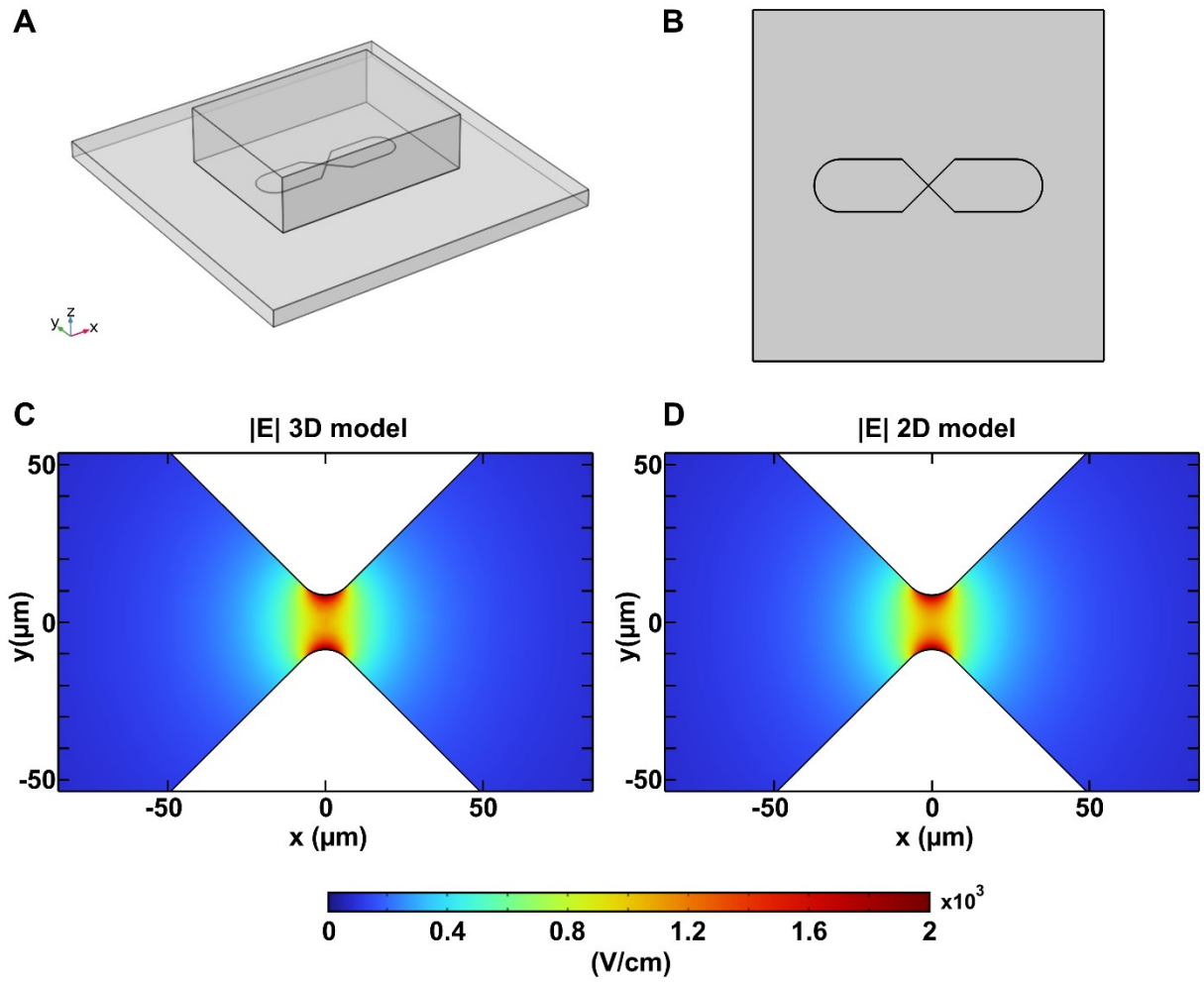


**Figure S2** Comparison for the electric behavior between a 3D and a 2D model for design 4. **(A)** 3D schematic of the model. **(B)** 2D version schematic of the model. **(C)** and **(D)** Electric field magnitude for the 3D and 2D models, respectively.

### 1.3 Joule heating evaluation

The 3D model was used to estimate and evaluate the claims that the electric field produced by the application of 30 V would not represent an issue regarding temperature rise in the system. For this, the Electric Currents and Creeping Flow interfaces were coupled with the Heat Transfers in Solids and Fluids interface through the Electromagnetic Heating in the Multiphysics interface. Figure S3 compares the maximum temperature in the devices with design 4 here presented (Figure S3A) and the temperature rise in a previous work with a commonly used device configuration (Figure S3B).[1] From Figure S3A it can be clearly seen that the temperature rise in the design produced in the present study is negligible and it remains constant throughout a time duration significantly longer (90 s) than that of the experiments performed in this study (20 s). The Joule heating configuration for the 3D model was similar to that done by Gallo-Villanueva et al.[1]

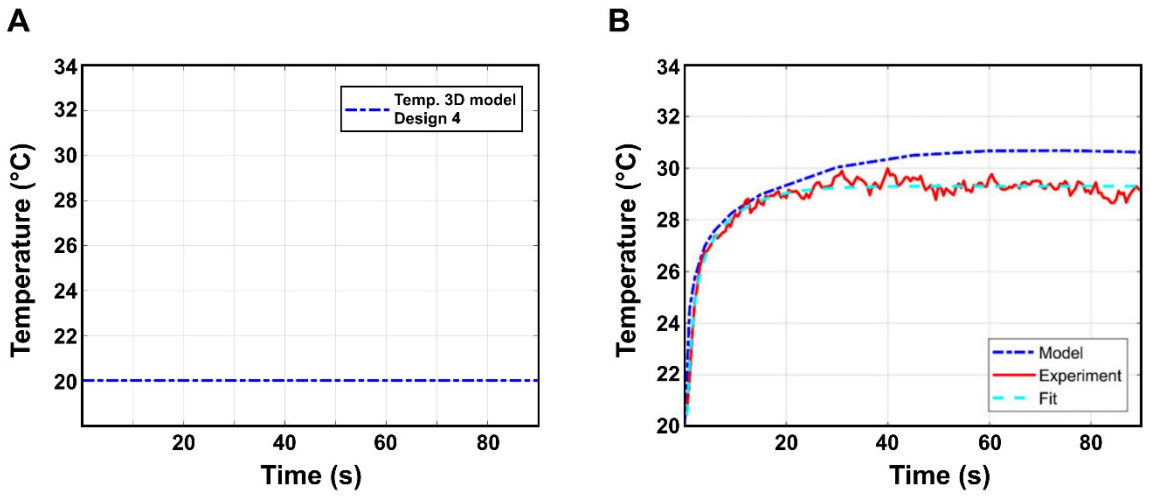


**Figure S3** Temperature modeling for design 4. (**A**) Temperature behavior for design 4 under the presented experimental conditions for a device with design 4 during 90 s. (**B**) Comparison to the results obtained by Gallo-Villanueva et al.[1], which is an example of commonly used designs and experimental conditions for DC-iEK systems. Reprinted with permission from John Wiley and Sons.

## 2. Microdevice fabrication

Microchannels were fabricated using a combination of both photolithography and soft lithography. Photolithography was used to fabricate the master mold, then PDMS microchannels were fabricated by conventional soft lithography.[2] For the master mold fabrication, SU-8 2025 negative photoresist (Kayaku Advanced Materials, Inc) was spin coated at 4000 rpm for 2 min over a 5 cm × 5 cm glass slide previously cleaned with acetone, isopropanol, and rinsed with DI water. The SU-8 coated glass slide was then soft baked on a hotplate for 5 min at a temperature of 95 °C. After that, a photomask imprinted with the channel design was placed over the coated slide and exposed to UV light (150-160 mJ/cm$^2$) for 4 s to start the crosslinking of SU-8. Then, the exposed slide was baked again at 95 °C for 2.5 min. Finally, the slide was submerged in SU-8 developer for 2 min to reveal the channel patterns on the slide, a 1 h hard bake process at 120 °C was performed to reduce cracks size and internal stress in the microchannel patterns. For the PDMS slab, a combination of 10 to 1 monomer and curing agent, respectively, was thoroughly mixed and then vacuumed until no bubbles were visible. Then the PDMS mixture was poured onto the master mold and let cure for 40 min at 95 °C on a hotplate. After that, the cured PDMS slab was trimmed, and a 1.5 mm-diameter biopsy puncher was used to punch holes at the ends of the microchannels for later reservoir connection. The PDMS slab with the microchannels were permanently bonded to a PDMS-coated glass slide to ensure material uniformity in all internal walls of the microchannel. The microchannel had dimensions of 1 cm long from inlet to outlet punched holes, 1 (or 3) mm wide, and ~30 μm tall.

### 3. Estimation of ion concentration from measured conductivity

For the suspending medium, the measured conductivity is indicating that a small amount of ions were present in the solution.[3–8] Considering the most likely ionic species molar concentrations in the order of tens of μM were expected,[7–10] similar to previous contributions.[11,12]

For the estimation of the ion concentration from measured conductivity the next relation of total dissolved solids (TDS) was applied:[7,8] $TDS \sim 0.5\sigma_m$ in mg/l in our case $TDS = 1.25$ mg/l. This is because even DI water can still contain a small amount of ions dissolved in it.[3–6,10] Assuming a similar distribution among the ions (as depicted in Table S3) would correspond to 0.3125 mg/l for each ion that can be readily related to a molar concentration.[9] This again, should allowed us to use the model proposed in the Theory section in the main document.

**Table S2** Estimation for the molar concentration

| TDS (mg/l) | Ion | Concentration (μM) |
|---|---|---|
| 0. 3125 | $K^{1+}$ | 8 |
| 0. 3125 | $Na^{1+}$ | 13.6 |
| 0. 3125 | $Mg^{2+}$ | 12.8 |
| 0. 3125 | $Ca^{2+}$ | 7.8 |

**4. Backflow estimation**

Backflow was calculated by the displaced volume due to EOF al the maximum applied electric field (1500 V/cm) as $Vol = u_{EO}At = \mu_{EO}E(H \cdot W)t$, where $A$ is cross-sectional area of the channel and $t$ is the voltage step running time taken as 5 s. This displaced volume should produce a water column of height $h$ at the pipette tip and there a pressure driven backflow. With this, $h_{bf} = Vol/\pi r_{tip}^{2}$, where $r_{tip}$ is the radius of the pipette tip at the top measured as 4 mm. This yields an $h_{bf} = 21.7$ µm. Now, due to the properties of water surface tension it is generated an upward pull on the water at the pipette tip which can be estimated as $h_{pull} = 2Tcos\theta/(\rho g r_{tip})$,[13] $T$ is the water surface tension (0.073 N/m), $\rho$ is the water density, and $\theta$ is the contact angle, taken as 89° which takes this estimation to a lower bound. With this $h_{pull} = 65$ µm, which is significantly larger that $h_{bf}$ meaning at that the pressure driven backflow is not even enough to overcome the fluid surface tension.

## 5. Experimental setup

Figure S4 shows the set up used for experiments.

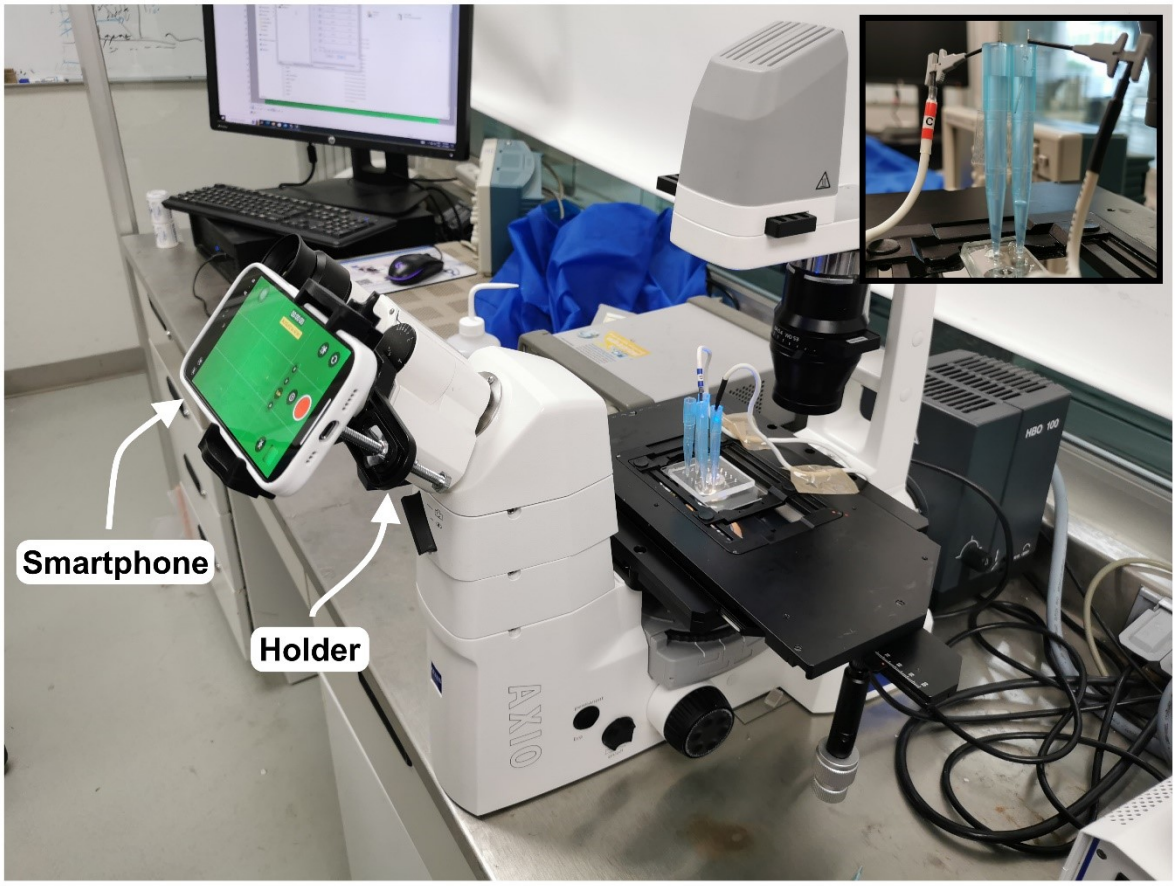


**Figure S4** Experimental setup. Microfluidic device mounted on the microscope stage. The inset shows a close-up of the electrical connections between the electrodes and the device reservoirs. Labels show the smartphone used for video capture and the holder used to fix it in position.

## 6. Example of PTV analysis of experimental data

Figure S5 exemplifies the experimental data analysis. First, experimental recordings are separated into 5 s sections containing the information corresponding to a certain applied electric field. The video undergoes analysis using ImageJ (NIH, USA) where particle velocity is obtained in small data sets presented in units of pixel per frame (px/fr), which is then converted (through a px-to-μm conversion factor) to micrometers per second (μm/s), which is then used to directly estimate the corresponding electrokinetic mobility using eqns (2) and (3). The px-to-μm conversion was performed by comparing experimental video snapshots to scaled micrographs of the system, while the time resolution was provided by the video frame rate: 60 frames per second or, equivalently, 16.666 ms per frame.

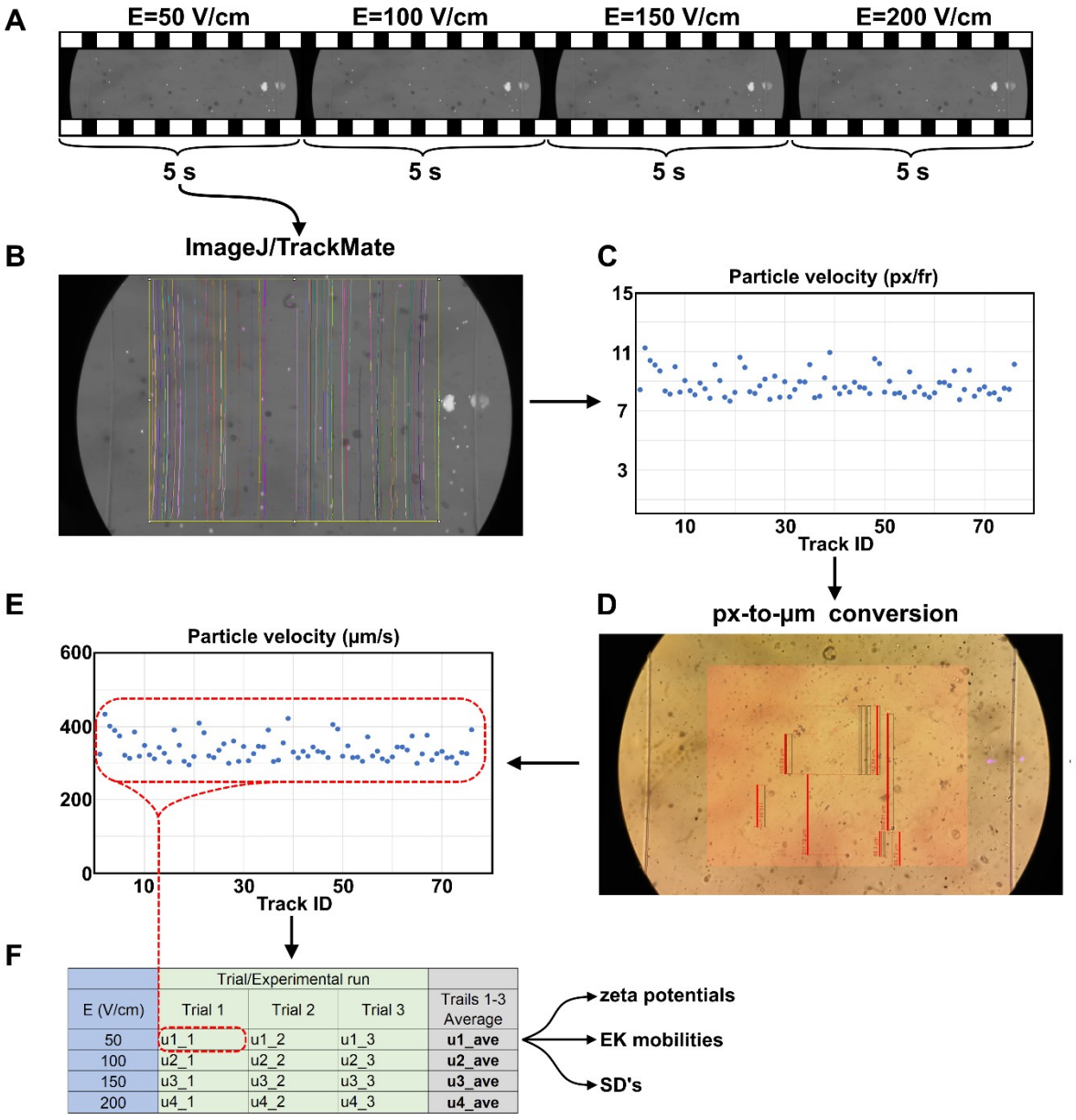


**Figure S5** Example of PTV analysis. **(A)** The experimental video was sectioned into 5 s sections that correspond to a certain applied electric field and therefore a certain particle velocity. **(B)** The video was analyzed using ImageJ/TrackMate and small data set was obtained. **(C)** The velocity was provided in units of px/fr. **(D)** A px-to-µm conversion factor was obtained when comparing experimental video snapshots to device scaled micrographs. **(E)** The velocity data was then presented in µm/s. **(F)** Data from all trial/experimental run and electric fields was collected and grouped to obtain relevant parameters (e.g., zeta potential, EK mobilities, standard deviations).

## 7. Example of visual determination of $E_{EEC}$

Figure S6 shows an example for the determination of the visual $E_{EEC}$ ($E_{EEC}^{vis}$). Figure S3 represents an overlay of the experimental snapshot and the numerical results of the electric field distribution inside two triangular geometry devices. Contour lines are used to delimit the trapping regions with a corresponding electric field intensity range.

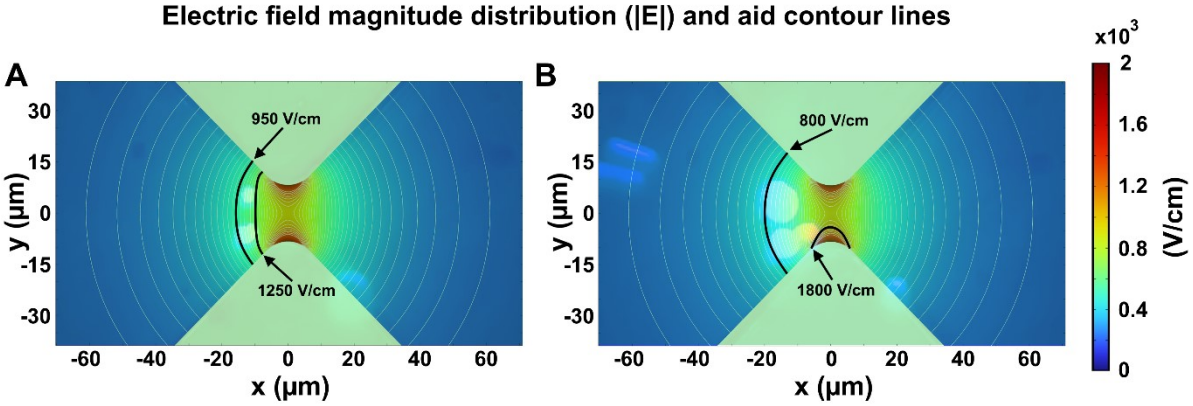


**Figure S6** Determination of $E_{EEC}$ by visual inspection performed on two different experimental runs (**A** and **B**) of a device with design 4.

**8. Validation of EOF via current monitoring.**

In order to support the $\zeta_w$ value obtained through PIV, the electroosmotic flow was also characterized using the technique of Current Monitoring as described by the Lapizco-Encinas group.[14] In short, three flat microfluidic channels filled with the suspending medium (~2 µS/cm) were connected in parallel to the power supply (LabSmith HVS448 6000D) and 200 V were applied during 20 s. LabSmith's Sequence software was used to monitor the current through the microfluidic channels during the first 20 s obtaining a characteristic current $I_a$. Then, one of the reservoirs for each microfluidic channel was emptied and filled with and auxiliary solution (~13 µS/cm) and the process was repeated obtaining a current slope and a second characteristic current $I_b$. As the geometric characteristics of the microchannel are known, the relation $\mu_{EO} = slope \cdot L/(E(I_b - I_a))$ can be used and compared to $\mu_{EO} = -\varepsilon_m \zeta_w/\eta$. This technique resulted in a $\zeta_w$ = 99.65 (±3) mV in comparison to $\zeta_w$ = 102.89 (±2) mV from PIV, which correspond to a difference of only 3%.

## 9. Plane of alignment for visual comparison of experiments and numerical results

As mentioned in the main document, due to the nature of the fabrication process, it is very difficult to produce devices with a perfectly vertical profile using photolithography. Figure S7A-B exemplifies this. Figure S7C shows a middle plane which is equivalent of taking the average dimensions of the fabricated devices. Such dimensions were the ones used in the model numerically simulated using COMSOL. In addition, Fig. S7 shows the reason why in Figures 3 and 4 we used a double white dashed line to delimit the triangle tip contour, as they delimit the upper and lower contour as depicted in Fig. S7.

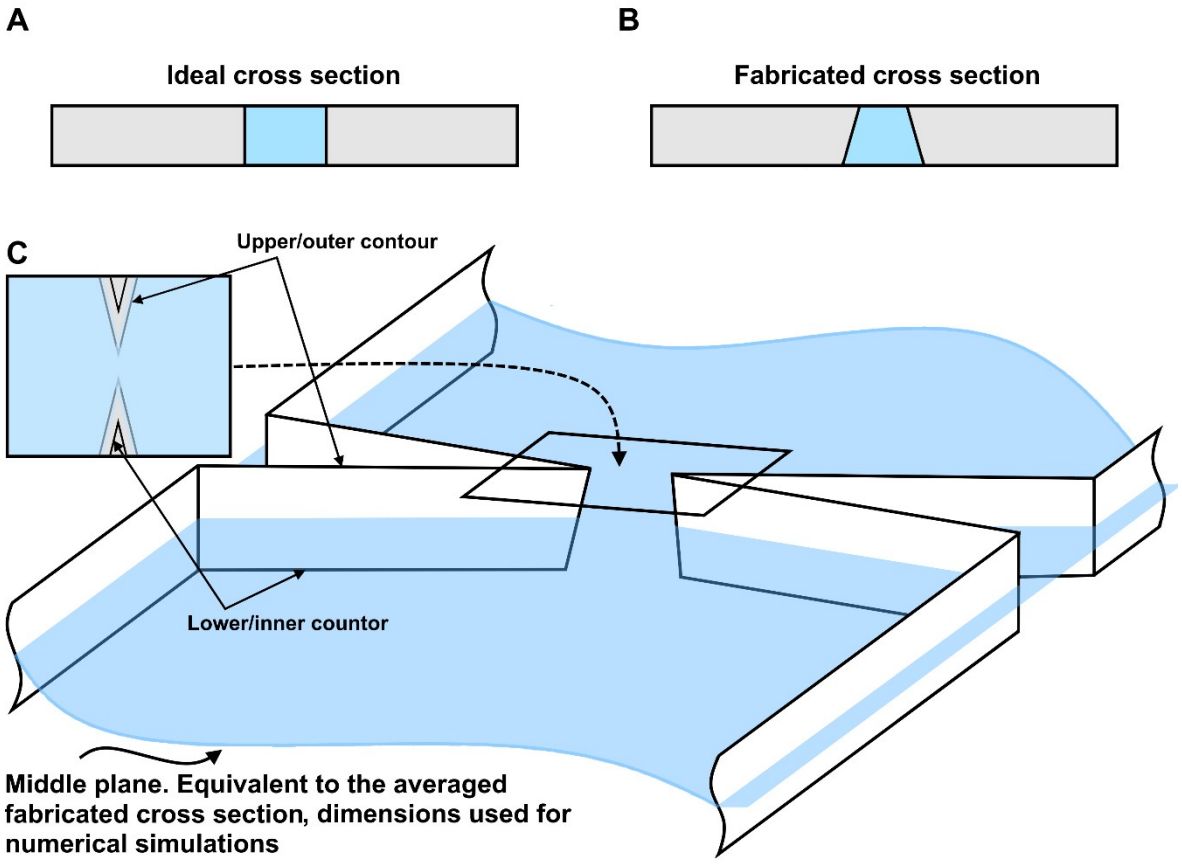


**Figure S7** Comparison of an ideal cross section (**A**) and an approximation for a fabricated cross section (**B**) and plane used for simulations (**C**).

## 10. Trapping region velocity and vector fields

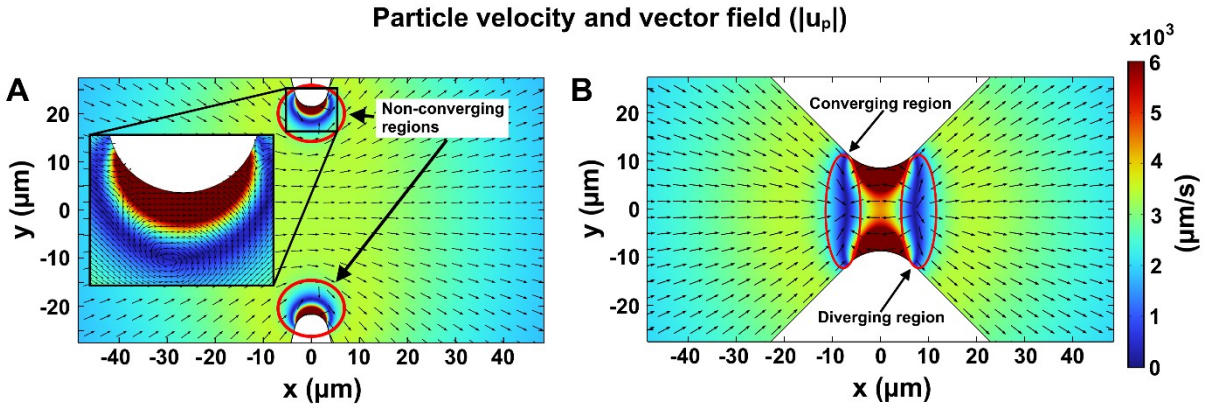


**Figure S8** Particle velocity and vector field. **(A)** Particle velocity and vector field for an instance of design 3. Showed in red ellipses are the trapping region marked as non-converging (i.e., unstable). **(B)** Particle velocity and vector field for an instance of design 4. Showed in red ellipses are the trapping region marked as converging (i.e., stable) and diverging (i.e., unstable) regions. Note that here non-converging does not necessarily mean diverging, only that no clear pattern for neither converging nor diverging is seen.

## 11. Particle velocity field for channel designs 1 and 2

Figure S9 shows the numerical results for the particle velocity field inside the channels with designs 1 and 2. From Fig. S9 it can be seen that only tiny and unstable trapping regions are predicted in design 1 (Fig. S9A) and no particle trapping is predicted for design 2 (Fig. S9B). This is in accordance with the experimentally observed, where no particle trapping was observed for these designs.

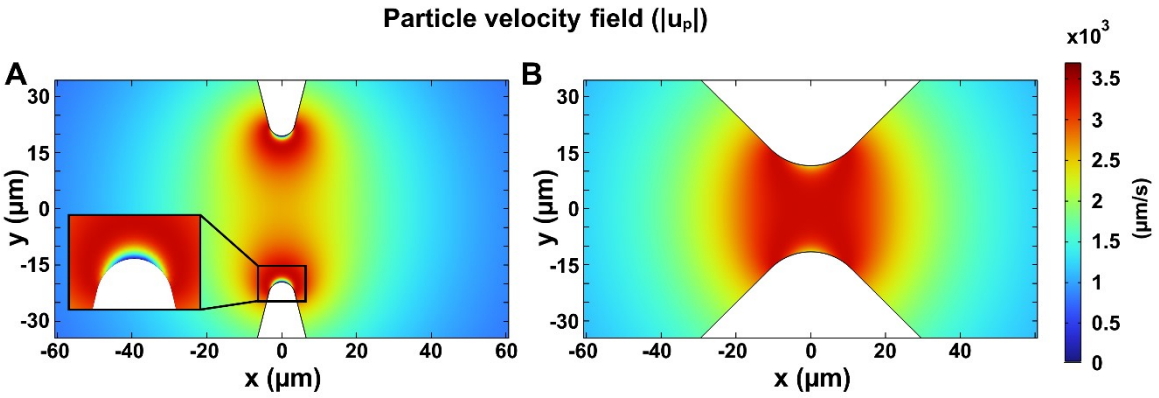


**Figure S9** Particle velocity field for channel designs 1 and 2. **(A)** Desing 1 could theoretically achieve particle trapping, however, only on tiny and unstable regions. **(B)** No particle trapping is predicted by the model in design 2.

## 12. Comparing maximum values for nonlinear electrophoretic velocity and dielectrophoretic velocity

**Table S3** Comparison of numerically obtained maximum values for $|u_{EP,NL}|$and $|u_{DEP}|$ for designs shown in Figures 3 and 5 in the main document.

| Design | Max $\|u_{EP,NL}\|$ (μm/s) | Max $\|u_{DEP}\|$ (μm/s) | $\|u_{DEP}\|/\|u_{EP,NL}\| * 100$ (%) |
|---|---|---|---|
| 3 (instance 1) | 50414 | 4860 | 9.6 |
| 3 (instance 2) | 81761 | 6697 | 8.19 |
| 4 (instance 1) | 42631 | 1722 | 4.02 |
| 4 (instance 2) | 47139 | 1899 | 4.03 |

## 13. Trapping region size comparison with previous work

Figure S10 shows a size comparison between a typical trapping region in DC-iEK device (Fig. S10A),[15] and the trapping region here presented (Fig. S10B) at the same scale. Figure S10C shows a zoom-in to the trapping region for better appreciation. From Fig. S10 it can be seen that the trapping regions here presented are significantly smaller, which can be translated to a more accurate visual determination of the EK characteristics of the particle. From the scaled micrograph, the particle trapping band can be measured and the reduction in size can be calculated, reducing from 60 µm to just 5 µm which represents a 12-fold reduction. This entails that the particle position can be more accurately determined and therefore the trapping electric field can also be more accurately localized and determined reducing uncertainty in the measurements.

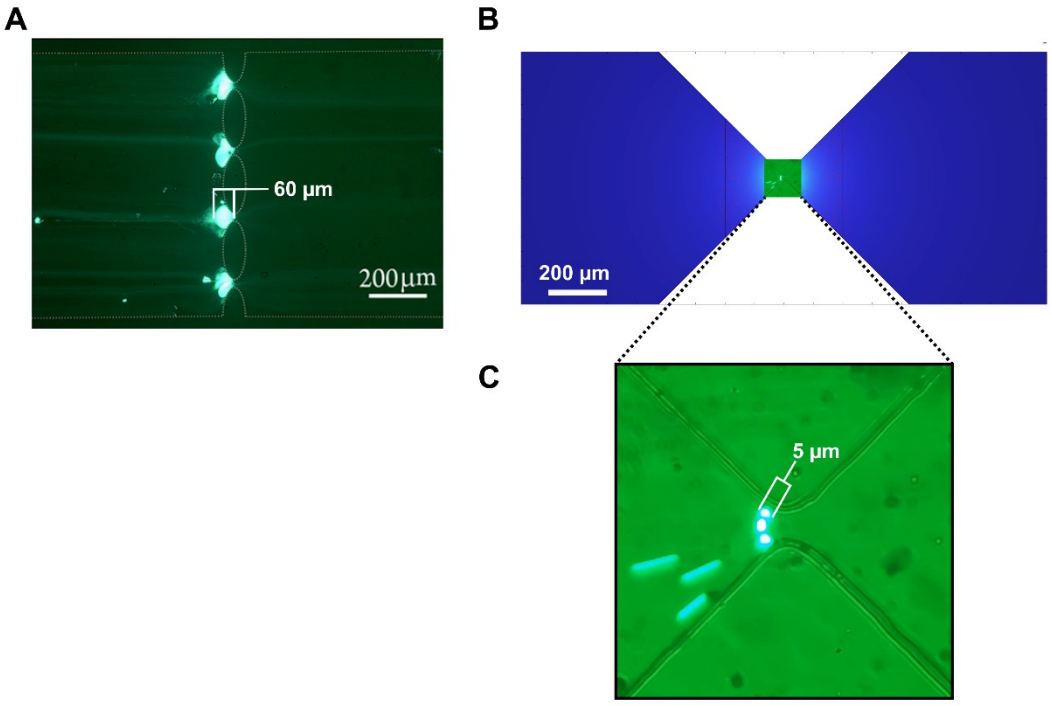


**Figure S10** Trapping region size comparison with previous work, **(A)** Perez-Gonzalez et al. [15], reprinted with permission from the American Chemical Society, **(B)** present work and **(C)** zoom-in to the trapping region. Reduction of the trapping region reduces the electric field range to be analyzed giving more precision to the determined values.

## References


(1) Gallo-Villanueva, R. C.; Perez-Gonzalez, V. H.; Cardenas-Benitez, B.; Jind, B.; Martinez-Chapa, S. O.; Lapizco-Encinas, B. H. Joule Heating Effects in Optimized Insulator-Based Dielectrophoretic Devices: An Interplay between Post Geometry and Temperature Rise. *Electrophoresis* **2019**, *40* (10), 1408–1416. https://doi.org/10.1002/elps.201800490.

(2) Xia, Y.; Whitesides, G. M. Soft-Lithography. *Angew. Chemie - Int. Ed.* **1998**, *37*, 550–575. https://doi.org/10.1002/(SICI)1521-3773(19980316)37:5<550::AID-ANIE550>3.0.CO;2-G.

(3) Islam, T.; Salamat, A.; Singh, S. K.; Rehman, M. A Cross-Conductive Sensor to Measure Bottled Water Quality. *Conf. Rec. - IEEE Instrum. Meas. Technol. Conf.* **2021**, *2021-May*, 0–5. https://doi.org/10.1109/I2MTC50364.2021.9459929.

(4) Corwin, D. L.; Yemoto, K. Salinity: Electrical Conductivity and Total Dissolved Solids. *Soil Sci. Soc. Am. J.* **2020**, *84* (5), 1442–1461. https://doi.org/10.1002/saj2.20154.

(5) Nguyen, M. D.; Rahman, M.; Wong, Y. S. Simultaneous Micro-EDM and Micro-ECM in Low-Resistivity Deionized Water. *Int. J. Mach. Tools Manuf.* **2012**, *54–55*, 55–65. https://doi.org/10.1016/j.ijmachtools.2011.11.005.

(6) *Conductivity Guide - Van London - pHoenix*. http://www.vl-pc.com/index.cfm/technical-info/conductivity-guide/ (accessed 2023-10-06).

(7) Rusydi, A. F. Correlation between Conductivity and Total Dissolved Solid in Various Type of Water: A Review. *IOP Conf. Ser. Earth Environ. Sci.* **2018**, *118* (1). https://doi.org/10.1088/1755-1315/118/1/012019.

(8) Tong, J.; Yang, J.; Hu, B. X.; Sun, H. Experimental Study on Soluble Chemical Transfer to Surface Runoff from Soil. *Environ. Sci. Pollut. Res.* **2016**, *23* (20), 20378–20387. https://doi.org/10.1007/s11356-016-7248-2.

(9) *Molecular Weight Search*. https://webbook.nist.gov/chemistry/mw-ser/ (accessed 2023-10-04).

(10) Azoulay, A.; Garzon, P.; Eisenberg, M. J.; Rd, C. Comparison of the Mineral Content of Tap Water and Bottled Waters. *J. Gen. Intern. Med.* **2001**, *16* (3), 168–175.

(11) Coll De Peña, A.; Miller, A.; Lentz, C. J.; Hill, N.; Parthasarathy, A.; Hudson, A. O.; Lapizco-Encinas, B. H. Creation of an Electrokinetic Characterization Library for the Detection and Identification of Biological Cells. *Anal. Bioanal. Chem.* **2020**, *402*, 3935–3945. https://doi.org/10.1007/s00216-020-02621-9.

(12) Cardenas-Benitez, B.; Jind, B.; Gallo-Villanueva, R. C.; Martinez-Chapa, S. O.; Lapizco-Encinas, B. H.; Perez-Gonzalez, V. H. Direct Current Electrokinetic Particle

Trapping in Insulator-Based Microfluidics: Theory and Experiments. *Anal. Chem.* **2020**, *92* (19), 12871–12879. https://doi.org/10.1021/acs.analchem.0c01303.

(13) Cengel, Y. A.; Cimbala, J. M. *Fluid Mechanics; Fundamental and Aplication*; 2014.

(14) Saucedo-Espinosa, M. A.; Lapizco-Encinas, B. H. Refinement of Current Monitoring Methodology for Electroosmotic Flow Assessment under Low Ionic Strength Conditions. *Biomicrofluidics* **2016**, *10* (3), 033104. https://doi.org/10.1063/1.4953183.

(15) Perez-Gonzalez, V. H.; Gallo-Villanueva, R. C.; Cardenas-Benitez, B.; Martinez-Chapa, S. O.; Lapizco-Encinas, B. H. Simple Approach to Reducing Particle Trapping Voltage in Insulator-Based Dielectrophoretic Systems. *Anal. Chem.* **2018**, *90* (7), 4310–4315. https://doi.org/10.1021/acs.analchem.8b00139.